

# High-Throughput Identification of Exfoliable Two-Dimensional Materials with Active Basal Planes for Hydrogen Evolution

Tong Yang, Jun Zhou, Ting Ting Song, Lei Shen, Yuan Ping Feng,\* and Ming Yang\*



Cite This: *ACS Energy Lett.* 2020, 5, 2313–2321



Read Online

ACCESS |



Metrics & More

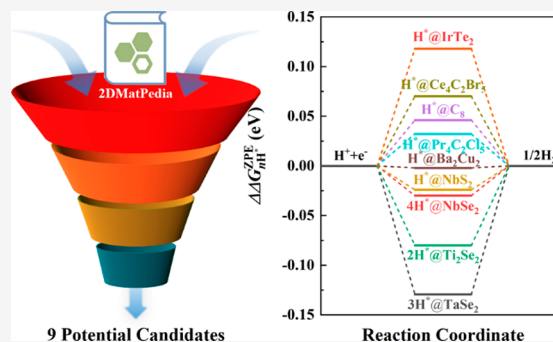


Article Recommendations



Supporting Information

**ABSTRACT:** Two-dimensional (2D) materials with intrinsically active basal planes are promising alternative catalysts to the Pt-group noble metals for large-scale hydrogen production. Herein, we perform a comprehensive screening of a 2D materials database (2DMatPedia) to identify such 2D catalysts for hydrogen evolution reaction (HER). Using the differential hydrogen adsorption Gibbs free energy as the thermodynamic descriptor, we report nine conducting, synthesizable, and exfoliable 2D catalysts with active basal planes ( $C_8$ ,  $NbS_2$ ,  $NbSe_2$ ,  $TaSe_2$ ,  $IrTe_2$ ,  $Ti_2Se_2$ ,  $Ba_2Cu_2$ ,  $Pr_4C_2Cl_5$ , and  $Ce_4C_2Br_5$ ), which may have an HER performance comparable to that of Pt-based catalysts. These 2D catalysts screened with high-throughput calculations provide a useful data set for further machine learning model construction or experimental examinations.



Electrocatalysis or photoelectrocatalysis is of great importance to the conversion and storage of renewable energies, which may facilitate the transition from the current fossil fuel-dominated energy system to a sustainable and environmentally friendly one in the future.<sup>1,2</sup> An intensively studied (photo)electrocatalytic process is hydrogen evolution reaction (HER), via which renewable electrical energies can be converted to the chemical energy in hydrogen, an energy-dense fuel and a feedstock for value-added chemicals (e.g., hydrocarbons and ammonia). To achieve a high conversion efficiency, HER catalysts play a key role. Pt-group noble metals have been found to exhibit the best performance to catalyze HER, but their scarcity and high cost hinder large-scale application. One practical route to lower the cost is to increase the utilization efficiency of these noble metals, such as alloying them with earth-abundant elements or downsizing the conventional nanoparticles to monolayers or single atoms.<sup>3–7</sup>

Another potential yet challenging route is to search for alternative earth-abundant catalysts. In this regard, two-dimensional transition metal dichalcogenides (TMDs), especially molybdenum disulfide ( $MoS_2$ ), have attracted tremendous attention since the catalytic performance of  $MoS_2$  was revealed.<sup>1,8,9</sup> However, their active sites are located only at the fractional edges, whereas the large basal planes are inert for HER. Hence, potential strategies have been reported to improve its catalytic performance by either maximizing the exposure of active edge sites or activating the inert basal plane,

such as vertically aligned growth,<sup>10</sup> phase or morphology engineering,<sup>11–15</sup> strain engineering,<sup>16</sup> surface vacancies or doping,<sup>16–20</sup> the formation of Janus structures,<sup>21,22</sup> and grain boundaries.<sup>23</sup> While these strategies can somewhat improve the catalytic performance and might be generalized to other catalyst candidates, the downside is the requirement of additional complicated treatments and hence higher costs. In addition to exploring more efficient optimization strategies, it is thus desirable to have 2D materials with intrinsically active basal planes, which could naturally provide a much higher density of active sites. Previous investigations have reported a few 2D materials with active basal planes such as TMDs (e.g.,  $1T-MoS_2$  and  $NbS_2$ ),<sup>11,24</sup> MXenes (e.g.,  $Ti_2CT_x$  and  $Ti_3C_2O_x$ ),<sup>25,26</sup> borophene or boride (e.g.,  $\alpha-MoB_2$ ),<sup>27,28</sup> and phosphates (e.g.,  $GeP_3$  and  $SnP_3$ ).<sup>29</sup> More recently, a high-throughput calculation has been conducted to screen 2D materials with active basal planes for HER applications from the 258 easily exfoliable candidates (inclusive of 97 metals).<sup>30</sup> Nevertheless, because of the rapid expansion of the 2D materials, more 2D materials have been realized in experi-

Received: May 3, 2020

Accepted: June 12, 2020

Published: June 12, 2020



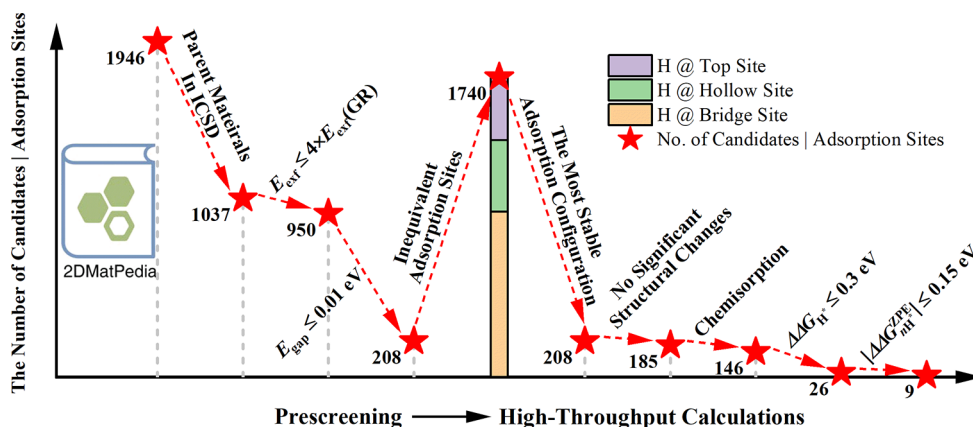


**Figure 1.** Prescreening and high-throughput screening scheme applied to the 2D materials from 2DMatPedia to identify potential 2D catalyst candidates with active basal planes toward HER. The total number of the exfoliated 2D materials in 2DMatPedia is 1946.  $E_{\text{exf}}^{\text{ref}}$  (GR) and  $E_{\text{gap}}$  are the exfoliation energy of graphene (in eV/atom) and the PBE band gap (in eV), respectively. Each candidate set is labeled as *Candidate Set-X*, where *X* is the set size. The stacked column shows the statistics on the inequivalent adsorption sites on the 2D materials in *Candidate Set-208*.

ments, e.g., SnSe,  $\text{Ca}_2\text{N}$ ,  $\text{Sb}_2\text{Se}_3$ ,  $\text{RuCl}_3$ ,  $\text{ZrTe}_3$ , and  $\text{IrTe}_2$ .<sup>31–34</sup> Recently, a new 2D materials database (2DMatPedia) has been built, which includes around 2000 monolayers exfoliated from layered bulk materials using a geometry-based algorithm without the constraint on the exfoliation energy (Figure S1).<sup>35–37</sup> With the development of experimental techniques, especially the recently developed gold tape method, those predicted 2D materials even with slightly high exfoliation energies can be expected to obtain in experiments soon.<sup>34,38,39</sup> Therefore, we carried out high-throughput first-principles calculations to screen 2D materials for HER applications from 2DMatPedia.

As Figure 1 illustrates, we first apply three criteria to prescreen 2D materials in 2DMatPedia. In the present study, we focus on only the layered materials that have been reported to be experimentally synthesizable at the current stage. Thus, whether the bulk layered parent materials can be found in the Inorganic Crystal Structure Database (ICSD) is the first prescreening criterion. This suggests 1037 2D materials in 2DMatPedia. The second criterion is the exfoliation energy,  $E_{\text{exf}}$ , which measures how feasibly a monolayer can be exfoliated from the corresponding layered bulk material. It is defined as  $E_{\text{exf}} = E_{\text{2D}} - E_{\text{bulk}}$ , where  $E_{\text{2D}}$  and  $E_{\text{bulk}}$  are the total energy per atom of a 2D material and its bulk counterpart, respectively.<sup>35,40,41</sup> In this step, we use four times the exfoliation energy of graphene,  $E_{\text{exf}}^{\text{ref}} = 4E_{\text{exf}}^{\text{ref}}(\text{GR}) = 268$  meV/atom, as the upper bound for the screening. Upon comparison with  $E_{\text{exf}}^{\text{ref}}$ , 950 materials are found, including some 2D materials which have been experimentally exfoliated from their bulk counterparts recently (e.g.,  $\text{RuCl}_3$ ,  $\text{MoS}_2$ , P, SnSe,  $\text{IrTe}_2$ , Sb, and  $\text{Ca}_2\text{N}$ ; see Table S1).<sup>31–34,42–47</sup> In addition, we further require the band gap ( $E_{\text{gap}}$ ) of the 2D materials to be  $E_{\text{gap}} \leq E_{\text{gap}}^{\text{ref}} = 0.01$  eV, because an excellent electrical conductivity is needed for high-performance electrochemical catalysts. Through the above prescreening criteria, 208 2D materials are identified as catalyst candidates toward HER, which are denoted as *Candidate Set-208* hereafter. Compared with the total of 92 2D metallic materials in the recent study,<sup>30</sup> our prescreened 2D catalyst candidates (208) represent a much larger data set because of a loose criterion on the exfoliation energy. It should be noted that in the above prescreening procedure,  $E_{\text{exf}}^{\text{ref}}$  and  $E_{\text{gap}}^{\text{ref}}$  are two tunable parameters, the change

of which can give different sizes of the screened data set. A higher exfoliation energy means that a layered material is more difficult to be exfoliated into 2D layers. As Figures 1 and S1 show,  $E_{\text{exf}}^{\text{ref}} = 4E_{\text{exf}}^{\text{ref}}(\text{GR})$  adopted here is high enough to include ~90% of the candidates. Further loosening this criterion may allow us to include more 2D materials such as the bismuth monolayer (bismuthene) which has a relatively high exfoliation energy of 281 meV/atom but has been exfoliated recently in the experiment.<sup>48</sup> As for the requirement on the electrical conductivity, decreasing  $E_{\text{gap}}^{\text{ref}}$  from 0.01 to 0.001 eV would filter out only three more 2D materials (see Table S2). It is noteworthy that the 2D materials containing noble metals are not excluded. For a 2D material with an active basal plane, the utilization efficiency of noble metals is much higher compared to the conventional nanoparticles.

Hydrogen evolution reaction involves both hydrogen adsorption (the Volmer step,  $\text{H}^+ + \text{e}^- \rightarrow \text{H}^*$ , where the asterisk denotes an adsorbed state) and desorption (the Heyrovsky step,  $\text{H}^* + \text{H}^+ + \text{e}^- \rightarrow \text{H}_2$ , or the Tafel step,  $2\text{H}^* \rightarrow \text{H}_2$ ). Either too strong or too weak hydrogen adsorption would decrease the overall reaction rate. For an optimal HER catalyst, the differential hydrogen adsorption Gibbs free energy has been found near zero in the computational hydrogen electrode (CHE) model developed by Nørskov et al.,<sup>8,49</sup> which can be expressed as

$$\Delta G_{(n-1)\text{H}^* + \text{H}^+ + \text{e}^- \rightarrow n\text{H}^*} = \Delta E + \Delta E_{\text{ZPE}} - T\Delta S + eU + k_{\text{B}}T(\ln 10)\text{pH}$$

$\Delta E$ , the differential hydrogen adsorption energy, is calculated as  $\Delta E = E_{n\text{H}^*} - E_{(n-1)\text{H}^*} - \frac{1}{2}E(\text{H}_2)$ , where  $E_{n\text{H}^*}$  and  $E(\text{H}_2)$  are the total energy of a given catalyst with *n* hydrogen adsorbates and the gas-phase  $\text{H}_2$ , respectively.  $\Delta E_{\text{ZPE}}$  and  $\Delta S$  are the change in the zero-point energy (ZPE) and the entropy (*S*) of hydrogen between the adsorbed and gas-phase state. *U* is the electrode potential, which is defined to be *U* = 0 V in the CHE model such that the protons and electrons are in equilibrium with the gas-phase  $\text{H}_2$  at standard conditions (temperature *T* = 298.15 K, pressure *P* = 1 bar, and pH=0). The last term is a free energy correction from a finite pH. In the present study, we evaluate the hydrogen evolution at standard conditions. Assuming the entropy of the hydrogen

adsorbate is negligible,  $T\Delta S \approx -\frac{1}{2}S_{\text{H}_2}^0 = -0.202$  eV, where  $S_{\text{H}_2}^0$  is the entropy of the gas-phase  $\text{H}_2$  at standard conditions.<sup>50</sup>

For brevity, we simplify  $\Delta G_{(n-1)\text{H}^*} + \text{H}^+ + e^- \rightarrow n\text{H}^*$  as  $\Delta G_{n\text{H}^*}$ . It should be noted that the calculated  $\Delta G_{n\text{H}^*}$  is dependent on the approximation to the exchange–correlation functional and the dispersive van der Waals interaction used in the calculations. We also note that Pt is currently recognized as the best HER catalyst, and the carbon-supported Pt nanoparticles have been widely used as a benchmark material in experiments.<sup>49,51</sup> Thus, the hydrogen adsorption Gibbs free energy relative to that of the Pt(111) surface (see section 9 in the Supporting Information) is used to theoretically benchmark the catalytic activity of a given catalyst candidate:  $\Delta\Delta G_{\text{H}^*} = \Delta G_{n\text{H}^*} - \Delta G_{4\text{H}^*}(\text{Pt})$ . In addition, the variation of  $\Delta E_{\text{ZPE}}$  is usually on the order of 0.01–0.1 eV for the hydrogen adsorption on different materials; thus, we first use the value of hydrogen adsorbed on Pt. The exact zero-point energy correction will then be calculated for the candidates in Tables 1 and S5 and used for the final round of screening.

**Table 1. Unit Cell Formula, Supercell Size, and the Hydrogen Adsorption Gibbs Free Energy ( $\Delta\Delta G_{\text{H}^*}$ ) for the 15 2D Catalyst Candidates in the Light Green Region in Figure 3, in Ascending Order of  $\Delta\Delta G_{\text{H}^*}$ <sup>a</sup>**

2DMatPedia ID	formula	supercell size	$\Delta\Delta G_{\text{H}^*}$ (eV)	$\Delta\Delta G_{\text{H}^*}^{\text{ZPE}}$ (eV)
2dm-3471	Hf <sub>3</sub> Te <sub>2</sub>	3 × 3	−0.290	−0.260
2dm-3665	Ba <sub>2</sub> N	2 × 2	−0.158	−0.194
2dm-3004	Ti <sub>2</sub> Se <sub>2</sub>	2 × 2	−0.154	−0.160
2dm-5357	C <sub>8</sub>	3 × 3	−0.104	0.046
2dm-3019	NbS <sub>2</sub>	3 × 3	−0.085	−0.024
2dm-4382	Pr <sub>4</sub> C <sub>2</sub> Cl <sub>5</sub>	3 × 2	0.034	0.032
2dm-5120	Ba <sub>2</sub> Cu <sub>2</sub>	2 × 2	0.050	−0.002
2dm-4339	Ce <sub>4</sub> C <sub>2</sub> Br <sub>5</sub>	3 × 1	0.090	0.070
2dm-4335	Cu <sub>2</sub> C <sub>2</sub> N <sub>4</sub>	3 × 1	0.101	0.238
2dm-3674	RuCl <sub>2</sub> O	3 × 3	0.104	0.239
2dm-3757	IrTe <sub>2</sub>	3 × 3	0.118	0.118
2dm-4076	Co <sub>4</sub> As <sub>4</sub> S <sub>4</sub>	2 × 2	0.196	0.251
2dm-3739	Te <sub>2</sub> Rh	3 × 3	0.238	0.233
2dm-4354	La <sub>4</sub> C <sub>2</sub> Br <sub>5</sub>	2 × 1	0.257	0.254
2dm-3520	Ca <sub>2</sub> Mn <sub>2</sub> Ge <sub>2</sub>	3 × 3	0.272	0.230

<sup>a</sup> $\Delta\Delta G_{\text{H}^*}^{\text{ZPE}}$  is the hydrogen adsorption Gibbs free energy corrected by the zero-point energy in the harmonic approximation.

For each catalyst candidate in *Candidate Set-208*, we considered hydrogen adsorption on all possible bridge, hollow, and top sites (via pymatgen).<sup>52</sup> Among them, 24 candidates have nonidentical top and bottom basal planes. For these candidates with asymmetric surfaces, hydrogen adsorption on both basal planes was taken into account. As Figure 1 shows, there are in total 1740 inequivalent possible adsorption sites, among which the bridge sites are dominant. We have performed high-throughput calculations to iterate over all the possible adsorption sites and identified the most energetically stable configuration of dilute hydrogen adsorption for each candidate.<sup>53–55</sup> In terms of the number of species, most of *Candidate Set-208* are binary and ternary compounds, and the rest are unary and quaternary compounds, as summarized in Table S4. Figure 2a shows the categorization of these candidates according to crystal systems at the symmetry precision (*symprec*) varying from  $1.0 \times 10^{-1}$  to  $1.0 \times 10^{-4}$ . In

addition to the intensively studied trigonal and hexagonal crystal structures, there are a variety of monoclinic, orthorhombic, and tetragonal crystal systems. The further symmetry analysis with the Spglib library reveals the space groups of the most dominant candidates: *P2<sub>1</sub>/m-10*, *P2<sub>1</sub>/m-11*, and *C2/m-12* for the monoclinic candidates; *Pmmn-59* for the orthorhombic candidates; *P4/mmm-123* and *P4/nmm-129* for the tetragonal candidates; *P3m1-164* for the trigonal candidates (see Figure S2).<sup>56</sup> These analyses highlight the structural diversity of the 2D candidates.

Regarding the hydrogen adsorption on the 2D materials in *Candidate Set-208*, we found that in the respective most energetically stable adsorption configuration, 23 candidates interact with the hydrogen adsorbate so strongly that it leads to a significant change in the entire atomic structures, a pronounced bond breaking, or even detachment of the atom from the 2D structures after hydrogen adsorption. We excluded such candidates and denoted the rest as *Candidate Set-185* (Figure 1). On the other hand, the hydrogen adsorption on some catalyst candidates falls into the physisorption regime, which is too weak to stabilize the hydrogen adsorbate for HER applications. Here the number of chemical bonds formed between the hydrogen adsorbate and each catalyst candidate in *Candidate Set-185* was counted. The atom of element M in a catalyst candidate is considered chemically bonded with the hydrogen adsorbate only if the M–H distance is smaller than the sum of their covalent radii,  $\langle r_{\text{cov}}(\text{M}) \rangle + \langle r_{\text{cov}}(\text{H}) \rangle$ .<sup>57</sup> The tolerance was set to an integer multiple of the standard deviation (*stdev*) of  $\langle r_{\text{cov}}(\text{M}) \rangle + \langle r_{\text{cov}}(\text{H}) \rangle$ . As Figure 2b shows, more than 50% of *Candidate Set-185* are thought of as the ones which have no chemical M–H bond in the most stable adsorption configuration if the tolerance is set to  $0 \times \text{stdev}$ . As the tolerance increases to  $1 \times \text{stdev}$ , the number of candidates without (with one) chemical M–H bond decreases (increases) significantly. Further increasing the tolerance leads to small variation in the chemical bond classification. However, for hydrogen adsorption on the FCC hollow site of the Pt(111) surface, the three Pt–H bonds cannot be identified until the tolerance is set up to  $3 \times \text{stdev}$  (see Table S3). Note that the chemical M–H bond length is unlikely to be greater than  $\langle r_{\text{cov}}(\text{M}) \rangle + \langle r_{\text{cov}}(\text{H}) \rangle + 3 \times \text{stdev}$  ( $\sim 0.15\%$ ), assuming a normal distribution. Therefore, we took the tolerance of  $3 \times \text{stdev}$ , and ruled out 39 candidates in *Candidate Set-185* without M–H bonds. The remaining 2D materials were termed *Candidate Set-146*. According to the number of the M–H bonds ( $n_{\text{M-H}}$ ), the hydrogen adsorption on most catalyst candidates energetically favors the top site ( $n_{\text{M-H}} = 1$ ), whereas the bridge site ( $n_{\text{M-H}} = 2$ ) and hollow site ( $n_{\text{M-H}} = 3, 4$ ) are rarely preferred.

Figure 3 shows the distribution of  $\Delta\Delta G_{\text{H}^*}$  for the dilute hydrogen adsorption on all catalyst candidates in *Candidate Set-146*. One can see that compared to the benchmark Pt (the dark green dashed line), the hydrogen adsorption in the most stable adsorption configuration is uphill in energy for  $\sim 90\%$  of the candidates. Among them, 82% are with  $\Delta\Delta G_{\text{H}^*} \geq 0.3$  eV, indicating that the basal plane of most catalyst candidates is catalytically inert for HER. Considering the variation of the zero-point energy (on the order of 0.01–0.1 eV), we focus on the 15 candidates with  $|\Delta\Delta G_{\text{H}^*}| \leq 0.3$  eV (the light green region in Figure 3) and calculate the respective zero-point energy correction to the hydrogen adsorption Gibbs free energy ( $\Delta\Delta G_{\text{H}^*}^{\text{ZPE}}$ ) in the harmonic approximation, as tabulated in Table 1.



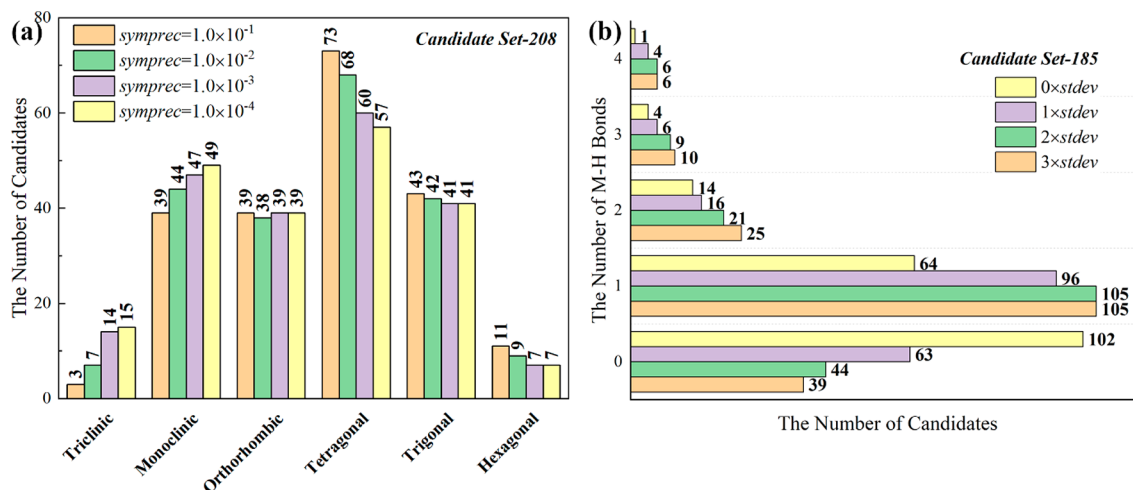


Figure 2. (a) Statistics on the crystal systems of *Candidate Set-208* at a series of symmetry precisions (*symprec*). (b) Number of chemical bonds between the hydrogen adsorbate and the catalyst candidates (M–H bonds) in *Candidate Set-185*, compared with  $\langle r_{\text{cov}}(\text{M}) \rangle + \langle r_{\text{cov}}(\text{H}) \rangle$ . M denotes the site of a candidate to which the hydrogen adsorbate binds. The tolerance is set to integer multiples of the standard deviation (*stdev*) of  $\langle r_{\text{cov}}(\text{M}) \rangle + \langle r_{\text{cov}}(\text{H}) \rangle$ .

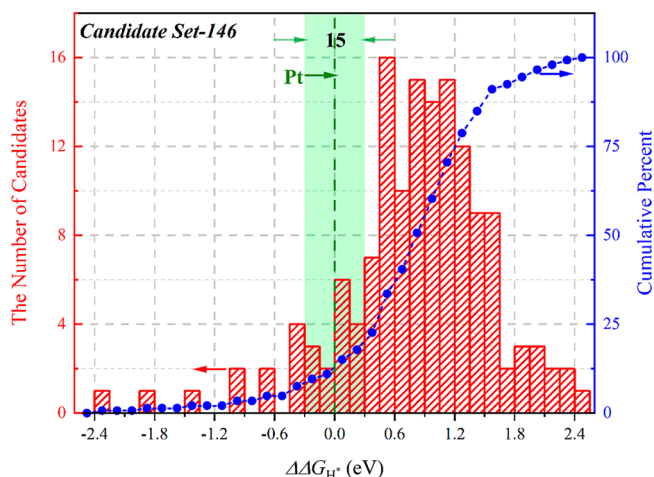


Figure 3. Distribution of the hydrogen adsorption Gibbs free energy ( $\Delta\Delta G_{\text{H}^*}$ ) on the catalyst candidates in *Candidate Set-146* in the most stable adsorption configuration.  $\Delta\Delta G_{\text{H}^*}$  is relative to that of Pt (the dark green dashed line), and the area with  $|\Delta\Delta G_{\text{H}^*}| \leq 0.3$  eV is shaded in light green.

According to thermodynamics, for a smaller  $|\Delta\Delta G_{\text{H}^*}^{\text{ZPE}}|$ , the performance of candidates is closer to Pt for catalyzing HER. Here we used  $|\Delta\Delta G_{\text{H}^*}^{\text{ZPE}}| \leq 0.15$  eV as the final screening criterion and identified six potential catalyst candidates (see

Table 1):  $\text{NbS}_2$  (−0.024 eV),  $\text{Ba}_2\text{Cu}_2$  (−0.002 eV),  $\text{Pr}_4\text{C}_2\text{Cl}_5$  (0.032 eV),  $\text{C}_8$  (0.046 eV),  $\text{Ce}_4\text{C}_2\text{Br}_5$  (0.070 eV), and  $\text{IrTe}_2$  (0.118 eV), on which hydrogen adsorption is nearly thermoneutral for HER at low hydrogen coverage. As Figure 4 shows,  $\text{C}_8$  (*Cmmm*-65),  $\text{Pr}_4\text{C}_2\text{Cl}_5$  (*Pmmm*-47), and  $\text{Ce}_4\text{C}_2\text{Br}_5$  are orthorhombic;  $\text{NbS}_2$  (*P6mm*-187) and  $\text{Ba}_2\text{Cu}_2$  (*P6/mmm*-191) are hexagonal;  $\text{IrTe}_2$  (*P3m1*-164) is trigonal. For  $\text{C}_8$  and  $\text{IrTe}_2$ , the most stable hydrogen adsorption is on top of C and Te of the outmost layer, respectively. For  $\text{NbS}_2$ , the hydrogen adsorbate favors the hollow site, forming three Nb–H bonds, whereas hydrogen is bound to three surface Ba atoms of  $\text{Ba}_2\text{Cu}_2$ . On the basal plane of  $\text{Pr}_4\text{C}_2\text{Cl}_5$  and  $\text{Ce}_4\text{C}_2\text{Br}_5$ , hydrogen is adsorbed on the M–M bridge site (M = Pr, Ce). It is worth noting that  $\text{NbS}_2$  has been experimentally proven with an efficient HER activity close to Pt, where the activity origin was confirmed to be the basal plane with an estimated turn over frequency (TOF) of  $0.95 \text{ s}^{-1}$ .<sup>24,58</sup> In ref 24,<sup>24</sup> the metallic 1T-TaS<sub>2</sub> was also studied, but is far inferior to  $\text{NbS}_2$  for catalyzing HER. In our calculations, 1T-TaS<sub>2</sub> was found unable to stabilize hydrogen for the Volmer step with  $\Delta\Delta G_{\text{H}^*} = 1.035$  eV. The agreement with the experimental results provides support for reliability of our high-throughput screening results.

With the calculated  $\Delta\Delta G_{\text{H}^*}$  for the catalyst candidates in *Candidate Set-146*, it is desirable to leverage such data to examine whether the hydrogen adsorption is simply correlated with a certain intrinsic property of a given material. Recently, it

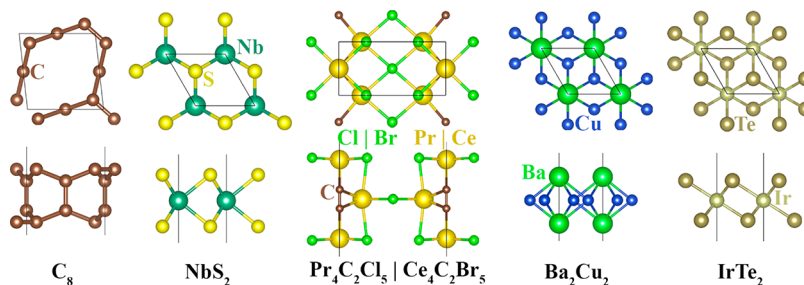


Figure 4. Top (top panel) and side (bottom panel) views of the six potential 2D catalyst candidates with  $|\Delta\Delta G_{\text{H}^*}^{\text{ZPE}}| \leq 0.15$  eV for dilute hydrogen adsorption. Note that the primitive unit cell of  $\text{C}_8$  has been used to evaluate its catalytic activity for HER. Its conventional unit cell ( $\text{C}_{16}$ ) is orthorhombic.

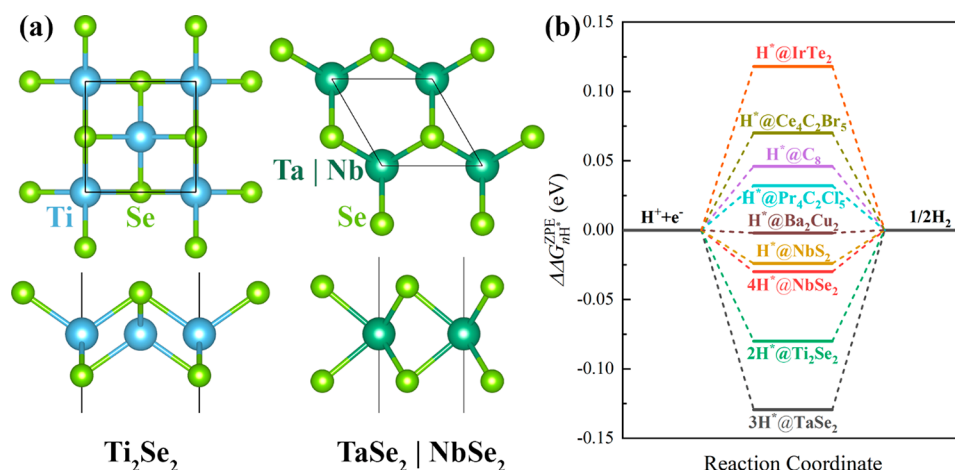


Figure 5. (a) Top (top panel) and side (bottom panel) views of  $\text{Ti}_2\text{Se}_2$ ,  $\text{TaSe}_2$ , and  $\text{NbSe}_2$ . (b) Gibbs free energy diagram for hydrogen evolution on the identified potential 2D catalyst candidates.

has been reported that the hydrogen adsorption strength on the basal plane of TMD linearly scales with the energy of the lowest unoccupied state ( $\epsilon_{\text{LUS}}$ ), while for metallic TMD edges, it is found to correlate with the d-band center of the edge-most metal site or the position of the p-states of the chalcogen site to which hydrogen is bound.<sup>24,59,60</sup> As Figures S5 and S6 show, however, it seems not to have a clear and simple correlation between  $\Delta\Delta G_{\text{H}^*}$  and any of the intrinsic properties mentioned above for our screened data set. This is understandable because such simple correlations were usually established on a series of adsorption systems bearing similar atomic structures, leading to the predominance of the electronic effect.<sup>24,59–62</sup> In contrast, the structural diversity of *Candidate Set-146* (Figures S3 and S4) as well as the variation of the local environment around the hydrogen adsorbate make the geometric effect another significant factor to determine the hydrogen adsorption strength in addition to the electronic effect. Notwithstanding, the calculation results for *Candidate Set-146* obtained here, at later time, might be a useful data set fed to train a machine learning model to reveal the complicated underlying correlation between hydrogen adsorption strength and the local coordination environment, as has been demonstrated on bimetallic and intermetallic facets.<sup>63,64</sup>

To the left of the light green region in Figure 3, the dilute hydrogen adsorption is too strong on 14 2D catalyst candidates with  $\Delta\Delta G_{\text{H}^*} < -0.15$  eV. More hydrogen atoms tend to adsorb on the basal plane of those candidates until it is thermodynamically unfavorable ( $\Delta\Delta G_{\text{H}^*} > 0$  eV). In this case, hydrogen coverage may have a significant impact on the catalytic activity toward HER, and the HER performance is mainly determined by the  $n$ th hydrogen adsorbate with closest-to-thermoneutral  $\Delta\Delta G_{\text{H}^*} \approx 0$  eV.<sup>5,8,49,51,65,66</sup> Bearing this in mind, a smaller supercell for each of the 14 candidates was used to investigate the hydrogen coverage effect. The calculated hydrogen coverage-dependent  $\Delta\Delta G_{\text{H}^*}^{\text{ZPE}}$  is summarized in Table S5. As the hydrogen coverage increases, the adsorption strength on  $\text{NbSe}_2$ ,  $\text{TaSe}_2$ , and  $\text{Ti}_2\text{Se}_2$  was weakened and close to that on the benchmark Pt, with  $\Delta\Delta G_{\text{H}^*}^{\text{ZPE}}(\text{NbSe}_2) = -0.030$  eV,  $\Delta\Delta G_{\text{H}^*}^{\text{ZPE}}(\text{TaSe}_2) = -0.129$  eV, and  $\Delta\Delta G_{\text{H}^*}^{\text{ZPE}}(\text{Ti}_2\text{Se}_2) = -0.080$  eV, respectively. This gives another three promising 2D catalysts for HER at the high hydrogen coverage regime. As Figure 5a shows, the structures of  $\text{NbSe}_2$  and  $\text{TaSe}_2$  are similar to  $\text{NbS}_2$ , while  $\text{Ti}_2\text{Se}_2$  has a

square lattice (space group:  $P4/nmm-129$ ). For the three potential candidates, the most stable adsorption is on the hollow site, where the hydrogen adsorbate is bound to the neighboring metal atoms in the middle layer ( $n_{\text{Ta/Nb-H}} = 3$ ;  $n_{\text{Ti-H}} = 4$ ). A sudden jump was observed in the hydrogen adsorption strength from  $\Delta\Delta G_{\text{H}^*}^{\text{ZPE}} < -0.15$  eV to  $\Delta\Delta G_{\text{H}^*}^{\text{ZPE}} > 0.15$  eV, with increasing H coverage, for  $\text{V}_6\text{O}_{13}$ ,  $\text{HoS}$ ,  $\text{Cu}_3\text{Se}_2\text{Cl}_2\text{O}_6$ , and  $\text{Ba}_2\text{N}$ , the structures of which are shown in Figures S7 and S8. Further investigations will be needed to evaluate their feasibility as HER catalysts. In particular,  $\text{Ba}_2\text{N}$  is well-known as a highly conductive electride.<sup>67</sup> The calculated electron localization function (ELF) in Figure S8 shows the electron accumulation right above the hollow site, which is also the most stable hydrogen adsorption site. The exfoliation of bulk electrides to 2D nanosheets has been experimentally demonstrated on  $\text{Ca}_2\text{N}$ , which has the same atomic arrangement as  $\text{Ba}_2\text{N}$ .<sup>32</sup> However, the electride such as  $\text{Ba}_2\text{N}$  is very reactive with either water or oxygen, which might be challenging for practical HER applications.

We also took  $\text{C}_8$  and  $\text{NbS}_2$  as two examples to check the hydrogen coverage effect. As discussed above, the dilute hydrogen adsorption (hydrogen coverage:  $\sim 11\%$ ) on these structures is very close to the thermoneutral adsorption on Pt. Different dependences on the hydrogen coverage are observed for  $\text{C}_8$  and  $\text{NbS}_2$ , as shown in Figure S9. For  $\text{C}_8$ , the hydrogen adsorption strength is weakly dependent on the hydrogen coverage, whereas the hydrogen adsorption strength on  $\text{NbS}_2$  is weakened by around 0.2 eV as the coverage increases. This can be ascribed to the difference in the favorite hydrogen adsorption site on  $\text{C}_8$  and  $\text{NbS}_2$ . For the former, hydrogen prefers to adsorb on top of the carbon atoms in the outmost layer ( $n_{\text{C-H}} = 1$ ). The binding mainly involves vertically aligned C  $p_z$  states, which is similar to that of the hydrogen adsorbed on  $\text{Mo}_6\text{S}_4$ .<sup>12</sup> In contrast, hydrogen adsorbed on the  $\text{NbS}_2$  monolayer is stabilized by the interaction with the laterally oriented d states of the three neighboring Nb atoms in the middle layer ( $n_{\text{Nb-H}} = 3$ ). Such a difference leads to a more pronounced coverage dependence for  $\text{NbS}_2$  compared to  $\text{C}_8$ . On the basis of this analysis, we may expect that hydrogen adsorption on  $\text{Ba}_2\text{Cu}_2$  ( $n_{\text{Ba-H}} = 3$ ),  $\text{Pr}_4\text{C}_2\text{Cl}_5$  ( $n_{\text{Pr-H}} = 2$ ), and  $\text{Ce}_4\text{C}_2\text{Br}_5$  ( $n_{\text{Pr-H}} = 2$ ) is also more sensitive to the hydrogen coverage and that hydrogen evolution on them is likely to occur at low coverage, while  $\text{IrTe}_2$  ( $n_{\text{Te-H}} = 1$ ) is less sensitive.

Thus, the strain engineering might be applicable to these coverage-sensitive catalyst candidates for further performance optimization.<sup>16,68</sup>

Among the nine identified potential HER catalyst candidates in the present study (Figure 5b), three group V transition metal dichalcogenides (group V TMDs: NbS<sub>2</sub>, NbSe<sub>2</sub>, and TaSe<sub>2</sub>) and IrTe<sub>2</sub> have been reported for HER applications.<sup>24,30,58,62,69–72</sup> As discussed above, NbS<sub>2</sub> has been experimentally proven active toward HER.<sup>24,58</sup> Texturized TaSe<sub>2</sub> flakes were also recently verified to be active toward HER in experiments, but it is inferior to NbS<sub>2</sub>.<sup>24,69</sup> Such a relative activity is in line with our theoretical calculations (Figure 5b). On the other hand, previous theoretical investigations on the basal plane activity of the group V TMDs seem to focus only on the atop chalcogen site, which led to an HER activity trend: NbS<sub>2</sub> ( $\Delta G_{H^*} = 0.12$  eV) > NbSe<sub>2</sub> ( $\Delta G_{H^*} = 0.54$  eV) > TaSe<sub>2</sub> ( $\Delta G_{H^*} = 0.65$  eV).<sup>70–72</sup> Thus, the observed HER activity of TaSe<sub>2</sub> in ref 69 is mainly ascribed to the active edges. Our calculations also suggest the similar hydrogen adsorption strength on top of the basal plane chalcogen sites:  $\Delta\Delta G_{H^*@S\ top\ site}(NbS_2) = 0.102$  eV >  $\Delta\Delta G_{H^*@Se\ top\ site}(NbSe_2) = 0.547$  eV >  $\Delta\Delta G_{H^*@Se\ top\ site}(TaSe_2) = 0.632$  eV. However, our iterations over all potential adsorption sites indicate that instead of the atop chalcogen site, the hollow site is the most stable hydrogen adsorption site:  $\Delta\Delta G_{H^*@hollow\ site}(NbS_2) = -0.085$  eV,  $\Delta\Delta G_{H^*@hollow\ site}(NbSe_2) = -0.309$  eV, and  $\Delta\Delta G_{H^*@hollow\ site}(TaSe_2) = -0.382$  eV, where the hydrogen adsorbate binds to three neighboring Nb or Ta atoms in the middle layer. As shown in Figure 5 and Table S5, the hydrogen coverage effect significantly affects the HER performance of NbSe<sub>2</sub> and TaSe<sub>2</sub>. It is noted that the optimal hydrogen adsorption on the hollow site of TaSe<sub>2</sub> (−0.129 eV) is comparable to that on the edge sites (Ta-edge, −0.16 eV; Se-edge, −0.10 eV).<sup>71</sup> Therefore, the observed HER activity of TaSe<sub>2</sub> in ref 69 is more likely contributed by both the edges and basal planes. As for IrTe<sub>2</sub>, a recent theoretical study showed that the weak hydrogen adsorption on the pristine basal plane can be enhanced by introducing vacancies.<sup>62</sup> Meanwhile, IrTe<sub>2</sub> was also predicted to be catalytically active toward CO<sub>2</sub> reduction reaction (CO<sub>2</sub>RR).<sup>73</sup> To reveal the selectivity of IrTe<sub>2</sub> between CO<sub>2</sub>RR and HER, microkinetic analysis will be further needed.<sup>74,75</sup> It should be noted that the family of 2D materials is still expanding; thus, we can expect that more 2D materials will be included in the database of 2D MatPedia later. Accordingly, this may result in other promising 2D materials-based electrocatalysts.

In summary, we report high-throughput first-principles calculations on the database of 2D MatPedia to screen high-performance exfoliable and synthesizable 2D catalysts with the active basal planes toward HER. Among 208 prescreened candidates, we find that the basal planes of NbS<sub>2</sub>, Ba<sub>2</sub>Cu<sub>2</sub>, C<sub>8</sub>, Pr<sub>4</sub>C<sub>2</sub>Cl<sub>5</sub>, Ce<sub>4</sub>C<sub>2</sub>Br<sub>5</sub>, IrTe<sub>2</sub>, NbSe<sub>2</sub>, Ti<sub>2</sub>Se<sub>2</sub>, and TaSe<sub>2</sub> exhibit thermodynamic capability of adsorbing hydrogen similar to that of Pt (Figure 5b), indicating their potential applications for catalyzing HER. The intrinsic HER performance of these potential candidates might be further optimized by using strain engineering.<sup>16,68</sup> These results will provide a useful data set for experimentalists to further scrutinize the predicted HER activity or for data scientists to construct machine learning models for HER performance predictions. We believe that the present study may contribute to an accelerated discovery of highly efficient HER catalysts for large-scale productions of

hydrogen and that the high-throughput screening scheme presented in this study may be generalized and applied to explore catalysts for other electrocatalytic processes.

## ■ ASSOCIATED CONTENT

### Supporting Information

The Supporting Information is available free of charge at <https://pubs.acs.org/doi/10.1021/acsenergylett.0c00957>.

Computational methods, statistics on the exfoliation energy, space group analysis, crystal system analysis, the correlation of  $\Delta\Delta G_{H^*}$  with  $\epsilon_{LUS}$ ,  $\langle E_{d-states} \rangle$  and  $\langle E_{p-states} \rangle$ , atomic structures, electron localization function of Ba<sub>2</sub>N, the exfoliation energy of some experimentally exfoliated candidate materials, candidate materials with a band gap between 0.01 and 0.001 eV, hydrogen adsorption on Pt, composition analysis, and hydrogen coverage-dependent  $\Delta\Delta G_{H^*}^{ZPE}$  (PDF)

## ■ AUTHOR INFORMATION

### Corresponding Authors

Yuan Ping Feng – Department of Physics and Centre for Advanced Two-Dimensional Materials, National University of Singapore, Singapore 117551 Singapore; [orcid.org/0000-0003-2190-2284](https://orcid.org/0000-0003-2190-2284); Email: [phyfyp@nus.edu.sg](mailto:phyfyp@nus.edu.sg)

Ming Yang – Institute of Materials Research and Engineering, Agency for Science, Technology and Research (A\*STAR), Innovis 138634, Singapore; [orcid.org/0000-0002-0876-1221](https://orcid.org/0000-0002-0876-1221); Email: [yangm@imre.a-star.edu.sg](mailto:yangm@imre.a-star.edu.sg)

### Authors

Tong Yang – Department of Physics, National University of Singapore, Singapore 117551 Singapore

Jun Zhou – Department of Physics, National University of Singapore, Singapore 117551 Singapore; [orcid.org/0000-0002-5505-7616](https://orcid.org/0000-0002-5505-7616)

Ting Ting Song – College of Physics and Space Science, China West Normal University, Nanchong 637002, China

Lei Shen – Department of Mechanical Engineering, National University of Singapore, Singapore 117575 Singapore; [orcid.org/0000-0001-6198-5753](https://orcid.org/0000-0001-6198-5753)

Complete contact information is available at: <https://pubs.acs.org/doi/10.1021/acsenergylett.0c00957>

### Notes

The authors declare no competing financial interest.

## ■ ACKNOWLEDGMENTS

This work used the computational resources of Centre for Advanced Two-Dimensional Materials and National Supercomputing Centre Singapore (NSCC). T.Y., J.Z., and Y.P.F. acknowledge the funding support from Academic Research Fund provided by Singapore Ministry of Education (Grant Nos.: MOE2018-T2-2-117 and R-144-000-413-114). M.Y. acknowledges funding support from A\*STAR Science and Engineering Research Council PHAROS 2D Program (SERC Grant No.: 152-70-00012) and The Accelerated Catalyst Development Platform (SERC Grant No.: A19E9a0103). L.S. acknowledges funding support from Singapore Ministry of Education (Grant No.: MOE R-265-000-691-114).



## REFERENCES

- (1) Seh, Z. W.; Kibsgaard, J.; Dickens, C. F.; Chorkendorff, I.; Nørskov, J. K.; Jaramillo, T. F. Combining theory and experiment in electrocatalysis: Insights into materials design. *Science* **2017**, 355 (6321), No. eaad4998.
- (2) Kibsgaard, J.; Chorkendorff, I. Considerations for the scaling-up of water splitting catalysts. *Nat. Energy* **2019**, 4 (6), 430–433.
- (3) Greeley, J.; Jaramillo, T. F.; Bonde, J.; Chorkendorff, I.; Nørskov, J. K. Computational high-throughput screening of electrocatalytic materials for hydrogen evolution. *Nat. Mater.* **2006**, 5 (11), 909–913.
- (4) Cao, Z.; Chen, Q.; Zhang, J.; Li, H.; Jiang, Y.; Shen, S.; Fu, G.; Lu, B.-a.; Xie, Z.; Zheng, L. Platinum-nickel alloy excavated nanomultipods with hexagonal close-packed structure and superior activity towards hydrogen evolution reaction. *Nat. Commun.* **2017**, 8 (1), 15131.
- (5) Yao, Y.; Gu, X.-K.; He, D.; Li, Z.; Liu, W.; Xu, Q.; Yao, T.; Lin, Y.; Wang, H.-J.; Zhao, C.; Wang, X.; Yin, P.; Li, H.; Hong, X.; Wei, S.; Li, W.-X.; Li, Y.; Wu, Y. Engineering the Electronic Structure of Submonolayer Pt on Intermetallic Pd<sub>3</sub>Pb via Charge Transfer Boosts the Hydrogen Evolution Reaction. *J. Am. Chem. Soc.* **2019**, 141 (S1), 19964–19968.
- (6) Fang, S.; Zhu, X.; Liu, X.; Gu, J.; Liu, W.; Wang, D.; Zhang, W.; Lin, Y.; Lu, J.; Wei, S.; Li, Y.; Yao, T. Uncovering near-free platinum single-atom dynamics during electrochemical hydrogen evolution reaction. *Nat. Commun.* **2020**, 11 (1), 1029.
- (7) Zhang, Z.; Feng, C.; Liu, C.; Zuo, M.; Qin, L.; Yan, X.; Xing, Y.; Li, H.; Si, R.; Zhou, S.; Zeng, J. Electrochemical deposition as a universal route for fabricating single-atom catalysts. *Nat. Commun.* **2020**, 11 (1), 1215.
- (8) Hinnemann, B.; Moses, P. G.; Bonde, J.; Jørgensen, K. P.; Nielsen, J. H.; Hørsh, S.; Chorkendorff, I.; Nørskov, J. K. Biomimetic Hydrogen Evolution: MoS<sub>2</sub> Nanoparticles as Catalyst for Hydrogen Evolution. *J. Am. Chem. Soc.* **2005**, 127 (15), 5308–5309.
- (9) Jaramillo, T. F.; Jørgensen, K. P.; Bonde, J.; Nielsen, J. H.; Hørsh, S.; Chorkendorff, I. Identification of Active Edge Sites for Electrochemical H<sub>2</sub> Evolution from MoS<sub>2</sub> Nanocatalysts. *Science* **2007**, 317 (5834), 100–102.
- (10) Wang, H.; Lu, Z.; Xu, S.; Kong, D.; Cha, J. J.; Zheng, G.; Hsu, P.-C.; Yan, K.; Bradshaw, D.; Prinz, F. B.; Cui, Y. Electrochemical tuning of vertically aligned MoS<sub>2</sub> nanofilms and its application in improving hydrogen evolution reaction. *Proc. Natl. Acad. Sci. U. S. A.* **2013**, 110 (49), 19701–19706.
- (11) Voiry, D.; Salehi, M.; Silva, R.; Fujita, T.; Chen, M.; Asefa, T.; Shenoy, V. B.; Eda, G.; Chhowalla, M. Conducting MoS<sub>2</sub> Nanosheets as Catalysts for Hydrogen Evolution Reaction. *Nano Lett.* **2013**, 13 (12), 6222–6227.
- (12) Yang, T.; Bao, Y.; Xiao, W.; Zhou, J.; Ding, J.; Feng, Y. P.; Loh, K. P.; Yang, M.; Wang, S. J. Hydrogen Evolution Catalyzed by a Molybdenum Sulfide Two-Dimensional Structure with Active Basal Planes. *ACS Appl. Mater. Interfaces* **2018**, 10 (26), 22042–22049.
- (13) Kibsgaard, J.; Jaramillo, T. F.; Besenbacher, F. Building an appropriate active-site motif into a hydrogen-evolution catalyst with thiomolybdate [Mo<sub>3</sub>S<sub>13</sub>]<sup>2−</sup> clusters. *Nat. Chem.* **2014**, 6 (3), 248–253.
- (14) Du, K.; Zheng, L.; Wang, T.; Zhuo, J.; Zhu, Z.; Shao, Y.; Li, M. Electrodeposited Mo<sub>3</sub>S<sub>13</sub> Films from (NH<sub>4</sub>)<sub>2</sub>Mo<sub>3</sub>S<sub>13</sub>·2H<sub>2</sub>O for Electrocatalysis of Hydrogen Evolution Reaction. *ACS Appl. Mater. Interfaces* **2017**, 9 (22), 18675–18681.
- (15) Bao, Y.; Yang, M.; Tan, S. J. R.; Liu, Y. P.; Xu, H.; Liu, W.; Nai, C. T.; Feng, Y. P.; Lu, J.; Loh, K. P. Substoichiometric Molybdenum Sulfide Phases with Catalytically Active Basal Planes. *J. Am. Chem. Soc.* **2016**, 138 (42), 14121–14128.
- (16) Li, H.; Tsai, C.; Koh, A. L.; Cai, L.; Contryman, A. W.; Fragapane, A. H.; Zhao, J.; Han, H. S.; Manoharan, H. C.; Abild-Pedersen, F.; Nørskov, J. K.; Zheng, X. Activating and optimizing MoS<sub>2</sub> basal planes for hydrogen evolution through the formation of strained sulphur vacancies. *Nat. Mater.* **2016**, 15 (1), 48–53.
- (17) Luo, Z.; Zhang, H.; Yang, Y.; Wang, X.; Li, Y.; Jin, Z.; Jiang, Z.; Liu, C.; Xing, W.; Ge, J. Reactant friendly hydrogen evolution interface based on di-anionic MoS<sub>2</sub> surface. *Nat. Commun.* **2020**, 11 (1), 1116.
- (18) Wang, X.; Zhang, Y.; Si, H.; Zhang, Q.; Wu, J.; Gao, L.; Wei, X.; Sun, Y.; Liao, Q.; Zhang, Z.; Ammarah, K.; Gu, L.; Kang, Z.; Zhang, Y. Single-Atom Vacancy Defect to Trigger High-Efficiency Hydrogen Evolution of MoS<sub>2</sub>. *J. Am. Chem. Soc.* **2020**, 142 (9), 4298–4308.
- (19) Yilmaz, G.; Yang, T.; Du, Y.; Yu, X.; Feng, Y. P.; Shen, L.; Ho, G. W. Stimulated Electrocatalytic Hydrogen Evolution Activity of MOF-Derived MoS<sub>2</sub> Basal Domains via Charge Injection through Surface Functionalization and Heteroatom Doping. *Adv. Sci.* **2019**, 6 (15), 1900140.
- (20) Shi, Y.; Zhou, Y.; Yang, D.-R.; Xu, W.-X.; Wang, C.; Wang, F.-B.; Xu, J.-J.; Xia, X.-H.; Chen, H.-Y. Energy Level Engineering of MoS<sub>2</sub> by Transition-Metal Doping for Accelerating Hydrogen Evolution Reaction. *J. Am. Chem. Soc.* **2017**, 139 (43), 15479–15485.
- (21) Er, D.; Ye, H.; Frey, N. C.; Kumar, H.; Lou, J.; Shenoy, V. B. Prediction of Enhanced Catalytic Activity for Hydrogen Evolution Reaction in Janus Transition Metal Dichalcogenides. *Nano Lett.* **2018**, 18 (6), 3943–3949.
- (22) Joo, P. H.; Zhang, J.; Yang, K. Size effects and odd–even effects on hydrogen adsorption on Janus MoSSe nanosheets: first-principles studies. *Mol. Syst. Des. Eng.* **2020**, 5 (4), 829–834.
- (23) Zhu, J.; Wang, Z.-C.; Dai, H.; Wang, Q.; Yang, R.; Yu, H.; Liao, M.; Zhang, J.; Chen, W.; Wei, Z.; Li, N.; Du, L.; Shi, D.; Wang, W.; Zhang, L.; Jiang, Y.; Zhang, G. Boundary activated hydrogen evolution reaction on monolayer MoS<sub>2</sub>. *Nat. Commun.* **2019**, 10 (1), 1348.
- (24) Liu, Y.; Wu, J.; Hackenberg, K. P.; Zhang, J.; Wang, Y. M.; Yang, Y.; Keyshar, K.; Gu, J.; Ogitsu, T.; Vajtai, R.; Lou, J.; Ajayan, P. M.; Wood, B. C.; Jakobson, B. I. Self-optimizing, highly surface-active layered metal dichalcogenide catalysts for hydrogen evolution. *Nat. Energy* **2017**, 2 (9), 17127.
- (25) Seh, Z. W.; Fredrickson, K. D.; Anasori, B.; Kibsgaard, J.; Strickler, A. L.; Lukatskaya, M. R.; Gogotsi, Y.; Jaramillo, T. F.; Vojvodic, A. Two-Dimensional Molybdenum Carbide (MXene) as an Efficient Electrocatalyst for Hydrogen Evolution. *ACS Energy Lett.* **2016**, 1 (3), 589–594.
- (26) Jiang, Y.; Sun, T.; Xie, X.; Jiang, W.; Li, J.; Tian, B.; Su, C. Oxygen-Functionalized Ultrathin Ti<sub>3</sub>C<sub>2</sub>T<sub>x</sub> MXene for Enhanced Electrocatalytic Hydrogen Evolution. *ChemSusChem* **2019**, 12 (7), 1368–1373.
- (27) Chen, Y.; Yu, G.; Chen, W.; Liu, Y.; Li, G.-D.; Zhu, P.; Tao, Q.; Li, Q.; Liu, J.; Shen, X.; Li, H.; Huang, X.; Wang, D.; Asefa, T.; Zou, X. Highly Active, Nonprecious Electrocatalyst Comprising Borophene Subunits for the Hydrogen Evolution Reaction. *J. Am. Chem. Soc.* **2017**, 139 (36), 12370–12373.
- (28) Shi, L.; Ling, C.; Ouyang, Y.; Wang, J. High intrinsic catalytic activity of two-dimensional boron monolayers for the hydrogen evolution reaction. *Nanoscale* **2017**, 9 (2), 533–537.
- (29) Wu, H.-H.; Huang, H.; Zhong, J.; Yu, S.; Zhang, Q.; Zeng, X. C. Monolayer triphosphates MP<sub>3</sub> (M = Sn, Ge) with excellent basal catalytic activity for hydrogen evolution reaction. *Nanoscale* **2019**, 11 (25), 12210–12219.
- (30) Karmodak, N.; Andreussi, O. Catalytic Activity and Stability of Two-Dimensional Materials for the Hydrogen Evolution Reaction. *ACS Energy Lett.* **2020**, 5 (3), 885–891.
- (31) Huang, Y.; Li, L.; Lin, Y.-H.; Nan, C.-W. Liquid Exfoliation Few-Layer SnSe Nanosheets with Tunable Band Gap. *J. Phys. Chem. C* **2017**, 121 (32), 17530–17537.
- (32) Druffel, D. L.; Kuntz, K. L.; Woomer, A. H.; Alcorn, F. M.; Hu, J.; Donley, C. L.; Warren, S. C. Experimental Demonstration of an Electride as a 2D Material. *J. Am. Chem. Soc.* **2016**, 138 (49), 16089–16094.
- (33) Fan, L.; Huang, D.; Wang, Y.; Miao, Z.; Ma, Y.; Zhao, Q.; Zha, Z. Cryo-assisted exfoliation of atomically thin 2D Sb<sub>2</sub>Se<sub>3</sub> nanosheets for photo-induced theranostics. *Chem. Commun.* **2019**, 55 (19), 2805–2808.

- (34) Huang, Y.; Pan, Y. H.; Yang, R.; Bao, L. H.; Meng, L.; Luo, H. L.; Cai, Y. Q.; Liu, G. D.; Zhao, W. J.; Zhou, Z.; Wu, L. M.; Zhu, Z. L.; Huang, M.; Liu, L. W.; Liu, L.; Cheng, P.; Wu, K. H.; Tian, S. B.; Gu, C. Z.; Shi, Y. G.; Guo, Y. F.; Cheng, Z. G.; Hu, J. P.; Zhao, L.; Yang, G. H.; Sutter, E.; Sutter, P.; Wang, Y. L.; Ji, W.; Zhou, X. J.; Gao, H. J. Universal mechanical exfoliation of large-area 2D crystals. *Nat. Commun.* **2020**, *11* (1), 2453.
- (35) Zhou, J.; Shen, L.; Costa, M. D.; Persson, K. A.; Ong, S. P.; Huck, P.; Lu, Y.; Ma, X.; Chen, Y.; Tang, H.; Feng, Y. P. 2DMPedia, an open computational database of two-dimensional materials from top-down and bottom-up approaches. *Sci. Data* **2019**, *6* (1), 86.
- (36) Zhou, J.; Shen, L.; Yang, M.; Cheng, H.; Kong, W.; Feng, Y. P. Discovery of Hidden Classes of Layered Electrides by Extensive High-Throughput Material Screening. *Chem. Mater.* **2019**, *31* (6), 1860–1868.
- (37) Jain, A.; Ong, S. P.; Hautier, G.; Chen, W.; Richards, W. D.; Dacek, S.; Cholia, S.; Gunter, D.; Skinner, D.; Ceder, G.; Persson, K. A. Commentary: The Materials Project: A materials genome approach to accelerating materials innovation. *APL Mater.* **2013**, *1* (1), 011002.
- (38) Tan, C.; Cao, X.; Wu, X.-J.; He, Q.; Yang, J.; Zhang, X.; Chen, J.; Zhao, W.; Han, S.; Nam, G.-H.; Sindoro, M.; Zhang, H. Recent Advances in Ultrathin Two-Dimensional Nanomaterials. *Chem. Rev.* **2017**, *117* (9), 6225–6331.
- (39) Liu, F.; Wu, W.; Bai, Y.; Chae, S. H.; Li, Q.; Wang, J.; Hone, J.; Zhu, X.-Y. Disassembling 2D van der Waals crystals into macroscopic monolayers and reassembling into artificial lattices. *Science* **2020**, *367* (6480), 903–906.
- (40) Choudhary, K.; Kalish, I.; Beams, R.; Tavazza, F. High-throughput Identification and Characterization of Two-dimensional Materials using Density functional theory. *Sci. Rep.* **2017**, *7* (1), 5179.
- (41) Ashton, M.; Paul, J.; Sinnott, S. B.; Hennig, R. G. Topology-Scaling Identification of Layered Solids and Stable Exfoliated 2D Materials. *Phys. Rev. Lett.* **2017**, *118* (10), 106101.
- (42) Cunningham, G.; Lotya, M.; Cucinotta, C. S.; Sanvito, S.; Bergin, S. D.; Menzel, R.; Shaffer, M. S. P.; Coleman, J. N. Solvent Exfoliation of Transition Metal Dichalcogenides: Dispersibility of Exfoliated Nanosheets Varies Only Weakly between Compounds. *ACS Nano* **2012**, *6* (4), 3468–3480.
- (43) O'Neill, A.; Khan, U.; Coleman, J. N. Preparation of High Concentration Dispersions of Exfoliated MoS<sub>2</sub> with Increased Flake Size. *Chem. Mater.* **2012**, *24* (12), 2414–2421.
- (44) Chen, Y.; Jiang, G.; Chen, S.; Guo, Z.; Yu, X.; Zhao, C.; Zhang, H.; Bao, Q.; Wen, S.; Tang, D.; Fan, D. Mechanically exfoliated black phosphorus as a new saturable absorber for both Q-switching and Mode-locking laser operation. *Opt. Express* **2015**, *23* (10), 12823.
- (45) Yasaei, P.; Kumar, B.; Foroozan, T.; Wang, C.; Asadi, M.; Tuschel, D.; Indacochea, J. E.; Klie, R. F.; Salehi-Khojin, A. High-Quality Black Phosphorus Atomic Layers by Liquid-Phase Exfoliation. *Adv. Mater.* **2015**, *27* (11), 1887–1892.
- (46) Ares, P.; Aguilar-Galindo, F.; Rodríguez-San-Miguel, D.; Aldave, D. A.; Díaz-Tendero, S.; Alcamí, M.; Martín, F.; Gómez-Herrero, J.; Zamora, F. Mechanical Isolation of Highly Stable Antimonene under Ambient Conditions. *Adv. Mater.* **2016**, *28* (30), 6332–6336.
- (47) Gibaja, C.; Rodríguez-San-Miguel, D.; Ares, P.; Gómez-Herrero, J.; Varela, M.; Gillen, R.; Maultzsch, J.; Hauke, F.; Hirsch, A.; Abellán, G.; Zamora, F. Few-Layer Antimonene by Liquid-Phase Exfoliation. *Angew. Chem., Int. Ed.* **2016**, *55* (46), 14345–14349.
- (48) Lu, L.; Liang, Z.; Wu, L.; Chen, Y.; Song, Y.; Dhanabalan, S. C.; Ponraj, J. S.; Dong, B.; Xiang, Y.; Xing, F.; Fan, D.; Zhang, H. Few-layer Bismuthene: Sonochemical Exfoliation, Nonlinear Optics and Applications for Ultrafast Photonics with Enhanced Stability. *Laser Photonics Rev.* **2018**, *12* (1), 1700221.
- (49) Nørskov, J. K.; Bligaard, T.; Logadottir, A.; Kitchin, J. R.; Chen, J. G.; Pandelov, S.; Stimming, U. Trends in the Exchange Current for Hydrogen Evolution. *J. Electrochem. Soc.* **2005**, *152* (3), J23–J26.
- (50) U.S. NIST. NIST Computational Chemistry Comparison and Benchmark Database. <http://cccbdb.nist.gov/>.
- (51) Skúlason, E.; Tripkovic, V.; Björketun, M. E.; Gudmundsdóttir, S.; Karlberg, G.; Rossmeisl, J.; Bligaard, T.; Jónsson, H.; Nørskov, J. K. Modeling the Electrochemical Hydrogen Oxidation and Evolution Reactions on the Basis of Density Functional Theory Calculations. *J. Phys. Chem. C* **2010**, *114* (42), 18182–18197.
- (52) Ong, S. P.; Richards, W. D.; Jain, A.; Hautier, G.; Kocher, M.; Cholia, S.; Gunter, D.; Chevrier, V. L.; Persson, K. A.; Ceder, G. Python Materials Genomics (pymatgen): A robust, open-source python library for materials analysis. *Comput. Mater. Sci.* **2013**, *68*, 314–319.
- (53) Kresse, G.; Hafner, J. Ab initio molecular dynamics for open-shell transition metals. *Phys. Rev. B: Condens. Matter Mater. Phys.* **1993**, *48* (17), 13115–13118.
- (54) Kresse, G.; Hafner, J. Ab initio molecular dynamics for liquid metals. *Phys. Rev. B: Condens. Matter Mater. Phys.* **1993**, *47* (1), 558–561.
- (55) Yang, T.; Yang, M.; Feng, Y. P. A Python Package for First-Principles High-throughput Calculations Using the Vienna Ab Initio Simulation Packages (VASP). [https://github.com/bitsoal/VASP-HTC\\_framework](https://github.com/bitsoal/VASP-HTC_framework).
- (56) Atsushi, T.; Isao, T. Spglib. <https://github.com/atsutogo/spglib>.
- (57) Cordero, B.; Gómez, V.; Platero-Prats, A. E.; Revés, M.; Echeverría, J.; Cremades, E.; Barragán, F.; Alvarez, S. Covalent radii revisited. *Dalton Trans* **2008**, No. 21, 2832–2838.
- (58) Zhang, J.; Wu, J.; Zou, X.; Hackenberg, K.; Zhou, W.; Chen, W.; Yuan, J.; Keyshar, K.; Gupta, G.; Mohite, A.; Ajayan, P. M.; Lou, J. Discovering superior basal plane active two-dimensional catalysts for hydrogen evolution. *Mater. Today* **2019**, *25*, 28–34.
- (59) Tsai, C.; Chan, K.; Abild-Pedersen, F.; Nørskov, J. K. Active edge sites in MoSe<sub>2</sub> and WSe<sub>2</sub> catalysts for the hydrogen evolution reaction: a density functional study. *Phys. Chem. Chem. Phys.* **2014**, *16* (26), 13156–13164.
- (60) Tsai, C.; Chan, K.; Nørskov, J. K.; Abild-Pedersen, F. Understanding the Reactivity of Layered Transition-Metal Sulfides: A Single Electronic Descriptor for Structure and Adsorption. *J. Phys. Chem. Lett.* **2014**, *5* (21), 3884–3889.
- (61) Xu, H.; Cheng, D.; Cao, D.; Zeng, X. C. A universal principle for a rational design of single-atom electrocatalysts. *Nat. Catal.* **2018**, *1* (5), 339–348.
- (62) Lee, J.; Kang, S.; Yim, K.; Kim, K. Y.; Jang, H. W.; Kang, Y.; Han, S. Hydrogen Evolution Reaction at Anion Vacancy of Two-Dimensional Transition-Metal Dichalcogenides: Ab Initio Computational Screening. *J. Phys. Chem. Lett.* **2018**, *9* (8), 2049–2055.
- (63) Ulissi, Z. W.; Tang, M. T.; Xiao, J.; Liu, X.; Torelli, D. A.; Karamad, M.; Cummins, K.; Hahn, C.; Lewis, N. S.; Jaramillo, T. F.; Chan, K.; Nørskov, J. K. Machine-Learning Methods Enable Exhaustive Searches for Active Bimetallic Facets and Reveal Active Site Motifs for CO<sub>2</sub> Reduction. *ACS Catal.* **2017**, *7* (10), 6600–6608.
- (64) Tran, K.; Ulissi, Z. W. Active learning across intermetallics to guide discovery of electrocatalysts for CO<sub>2</sub> reduction and H<sub>2</sub> evolution. *Nat. Catal.* **2018**, *1* (9), 696–703.
- (65) Strmcnik, D.; Tripkovic, D.; van der Vliet, D.; Stamenkovic, V.; Marković, N. M. Adsorption of hydrogen on Pt(111) and Pt(100) surfaces and its role in the HOR. *Electrochem. Commun.* **2008**, *10* (10), 1602–1605.
- (66) Tang, Q.; Jiang, D.-e. Mechanism of Hydrogen Evolution Reaction on 1T-MoS<sub>2</sub> from First Principles. *ACS Catal.* **2016**, *6* (8), 4953–4961.
- (67) Walsh, A.; Scanlon, D. O. Electron excess in alkaline earth subnitrides: 2D electron gas or 3D electride? *J. Mater. Chem. C* **2013**, *1* (22), 3525–3528.
- (68) Voiry, D.; Yamaguchi, H.; Li, J.; Silva, R.; Alves, D. C. B.; Fujita, T.; Chen, M.; Asefa, T.; Shenoy, V. B.; Eda, G.; Chhowalla, M. Enhanced catalytic activity in strained chemically exfoliated WS<sub>2</sub> nanosheets for hydrogen evolution. *Nat. Mater.* **2013**, *12* (9), 850–855.
- (69) Najafi, L.; Bellani, S.; Oropesa-Nuñez, R.; Martín-García, B.; Prato, M.; Pasquale, L.; Panda, J.-K.; Marvan, P.; Sofer, Z.; Bonaccorso, F. TaS<sub>2</sub>, TaSe<sub>2</sub>, and Their Heterogeneous Films as



Catalysts for the Hydrogen Evolution Reaction. *ACS Catal.* **2020**, *10* (5), 3313–3325.

(70) Pan, H. Metal Dichalcogenides Monolayers: Novel Catalysts for Electrochemical Hydrogen Production. *Sci. Rep.* **2015**, *4* (1), 5348.

(71) Tsai, C.; Chan, K.; Nørskov, J. K.; Abild-Pedersen, F. Theoretical insights into the hydrogen evolution activity of layered transition metal dichalcogenides. *Surf. Sci.* **2015**, *640*, 133–140.

(72) Chia, X.; Ambrosi, A.; Lazar, P.; Sofer, Z.; Pumera, M. Electrocatalysis of layered Group 5 metallic transition metal dichalcogenides ( $\text{MX}_2$ , M = V, Nb, and Ta; X = S, Se, and Te). *J. Mater. Chem. A* **2016**, *4* (37), 14241–14253.

(73) Shin, H.; Ha, Y.; Kim, H. 2D Covalent Metals: A New Materials Domain of Electrochemical  $\text{CO}_2$  Conversion with Broken Scaling Relationship. *J. Phys. Chem. Lett.* **2016**, *7* (20), 4124–4129.

(74) Liu, X.; Xiao, J.; Peng, H.; Hong, X.; Chan, K.; Nørskov, J. K. Understanding trends in electrochemical carbon dioxide reduction rates. *Nat. Commun.* **2017**, *8* (1), 15438.

(75) Zhong, M.; Tran, K.; Min, Y.; Wang, C.; Wang, Z.; Dinh, C.-T.; De Luna, P.; Yu, Z.; Rasouli, A. S.; Brodersen, P.; Sun, S.; Voznyy, O.; Tan, C.-S.; Askerka, M.; Che, F.; Liu, M.; Seifitokaldani, A.; Pang, Y.; Lo, S.-C.; Ip, A.; Ulissi, Z.; Sargent, E. H. Accelerated discovery of  $\text{CO}_2$  electrocatalysts using active machine learning. *Nature* **2020**, *581* (7807), 178–183.